Article

Mingled MnO$_2$ and Co$_3$O$_4$ Binary Nanostructures on Well-Aligned Electrospun Carbon Nanofibers for Nonenzymatic Glucose Oxidation and Sensing

Ziyu Yin, Kokougan Allado, Alex T. Sheardy, Zuowei Ji, Durga Arvapalli, Mengxin Liu, Peng He, Xinping Zeng,* and Jianjun Wei*

Cite This: *Cryst. Growth Des.* 2021, 21, 1527−1539

Read Online

ACCESS | Metrics & More | Article Recommendations | SI Supporting Information

ABSTRACT: This work reports on uniformly mingled nanostructures of Co$_3$O$_4$ and MnO$_2$ deposited on a well-aligned electrospun carbon nanofiber (WA-ECNF) mat for rapid glucose electrooxidation and sensing. The hybridization of Co$_3$O$_4$ and MnO$_2$ is synthesized by a simple one-step and template-free electrodeposition technique with a constant low current at 60 μA for 3 h at room temperature in an aqueous solution. The binary MnO$_2$/Co$_3$O$_4$@WA-ECNF nanomatrix electrode exhibits excellent uniformity with high porosity, increased electrochemically active surface areas and conductivity, fast charge transfer, and improved efficiency for glucose electrooxidation in comparison to the monometallic MnO$_2$ or Co$_3$O$_4$ at the WA-ECNFs. The electrochemical performance of the MnO$_2$/Co$_3$O$_4$@ECNF electrode is characterized by cyclic voltammetry (CV), electrochemical impedance spectroscopy (EIS), and chronoamperometry (CA). The MnO$_2$/Co$_3$O$_4$@ECNF electrode shows superior sensing characteristics including a rapid glucose oxidation response within 5 s, a wide range of detection from 5 μM to 10.9 mM, an excellent sensitivity of 1159 μA mM^{-1} cm^{-2}, and a detection limit of 0.3 μM (S/N = 3) with satisfactory selectivity, great reproducibility, and stability. These results are discussed with mechanisms of glucose absorption to the nanostructure surfaces followed by a fast glucose oxidation reaction.
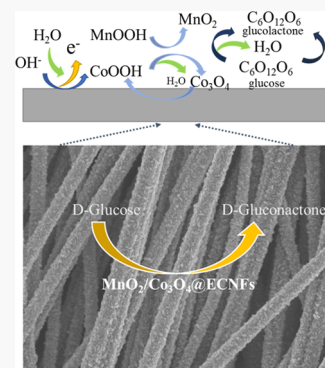
INTRODUCTION

Electrochemical glucose biosensors occupy a substantial portion in current blood glucose testing, clinical diagnosis, pharmaceutical analysis, and environmental monitoring owing to their rapid response, high sensitivity and selectivity, excellent stability, and reproducibility. While enzymatic glucose sensors have superb sensitivity and selectivity, which also dominate the major commercial market currently, they suffer from some intrinsic weaknesses including high cost, insufficient chemical and thermal stability, operating temperature limitations, and short shelf lifetime. These are associated with the structure and properties of the immobilized enzymes (e.g., glucose oxidase and/or dehydrogenase) and surrounding environments, such as pH, humidity, oxygen, temperature, and toxic chemicals.[1,2] Therefore, the development of non-enzymatic glucose sensors for reliable and fast detection has received special attention in overcoming the aforementioned shortcomings of enzyme-based glucose sensors.

Nonenzymatic glucose sensors are generally operated by a direct electrocatalytic oxidation of glucose at an electrode surface, which is modified with functional materials as a replacement of enzymes.[2] Noble metals and alloy nanoparticles show high electrocatalytic activity toward glucose oxidation;[1] however, they still suffer from sluggish kinetics and serious deactivation due to surface poisoning and fouling from intermediates or chloride ion adsorption.[3,4] Herein, versatile transition-metal oxides have been considered as one of the most promising catalysts for glucose detection,[5] energy storage, and conversion,[6,7] owing to their low cost, good biocompatibility, and excellent electrocatalytic activity. These metal oxides that have been studied include MnO$_2$,[8−10] Co$_3$O$_4$,[11−13] NiO,[14,15] and CuO.[16−18] Among these nonprecious metal oxide catalysts, MnO$_2$ has multiple crystallographic phases based on its tunnel structure,[10,19] which is recognized as an environmentally friendly electrocatalyst possessing high catalytic activity, good stability against corrosion, and abundant earth reserves.[20,21] The Co$_3$O$_4$-based nanocomposites enjoy outstanding electrocatalytic activity and stability because the cobalt ions possess d-band electrons exhibiting a similar property as the noble metals.[11,22] The diversiform d-orbitals in cobalt ions endow more dynamic d-electrons on the surface with highly active sites for electrocatalysis.[23] More importantly, multimetal oxides demonstrate improved catalytic activity compared to monometallic oxides. This can be ascribed to the

interfacial synergistic effect, potential complementary benefits, as well as combined compositions and structures for stabilizing an appropriate electronic configuration in high-efficiency electrocatalysts.[24,25] Recently, Mn/Co oxide catalysts showed excellent electrocatalytic activity that is superior to single metal oxides by providing more highly active sites and charge storage properties.[20,24] Sinha et al.[26] obtained a hybridized structure from 1D α-MnO_2 nanorods and Co_3O_4 nanoparticles and explored its glucose-sensing application. Their work achieved a sensitivity of 127 $\mu A\ mM^{-1}\ cm^{-2}$, a detection range of 60 μM to 7 mM, and a detection limit of 0.03 μM.

Even with such superior electrocatalytic activities, the intrinsic low electronic conductivity of metal oxides leads to a poor efficiency in electrocatalysis and limits the applications in electrochemistry. To overcome this drawback, some efforts have been made to construct a hybrid microelectrode that incorporates nanostructured metal oxides with high electrically conductive materials, including carbon materials,[12,27,28] metal–organic frameworks,[29,30] and conducting polymers.[18,31] Among these materials, the electrospun carbon nanofiber (ECNF) is considered to be a potentially promising candidate due to its large porosity, high conductivity, and inexpensive production with a freestanding nature.[32,33] Electrospinning is a simple, efficient, and scalable method, which utilizes an electrical force to draw charged threads of polymer solution or polymer melt followed by thermal treatment to create porous carbon nanofibers.[34] Especially, the well-aligned ECNF (WA-ECNF) structure could be utilized as a good scaffold to support uniformly coated metal oxide nanostructures. Such an aligned structure may shorten the distance of electron transport, therefore enhancing the electrodeposition rate of metal oxides.[27] Besides, introducing carboxyl groups on the ECNF surface can promote the nucleation of nanostructured metal oxides and bond well with conductive supports.[35] Meanwhile, ECNFs with large amounts of edge-plane-like defective sites are expected to show an attractive electrocatalytic property.[36] One can expect that WA-ECNFs combined with mingled nanostructured metal oxides will provide improved conductivity and electrocatalytic activity regarding applications in electrochemical sensing.

In this work, nanostructured MnO_2/Co_3O_4@ECNFs were synthesized by a facile one-step electrodeposition technique with a low constant current at 60 μA for 3 h to co-wrap MnO_2 and Co_3O_4 onto the surface of WA-ECNFs. Such a new hybrid nanocomposite electrode not only forms mesoporous surface features[37] but also renders innovations of mingled binary metal oxides aligned to the conductive carbon nanofiber for facilitating ion diffusion and charge transfer, thus improving electrocatalytic performance.[38,39] The fully characterized MnO_2/Co_3O_4@ECNFs were used for the electrocatalytic oxidation of glucose and as a superior nonenzymatic glucose sensor. Indeed, in a parallel comparative study with monometallic oxides electrodeposited onto WA-ECNFs, i.e., MnO_2@ECNF and Co_3O_4@ECNF electrodes, the results show that the binary MnO_2/Co_3O_4@ECNF electrode exhibits a much better performance in terms of electronic conductivity, large active site surface area, superb ratio of surface to volume, ion diffusion, and charge-transport ability in glucose oxidation and sensing applications. The MnO_2/Co_3O_4@ECNF hybrid nanoelectrode was directly applied to test the glucose concentration without any sonication or dissolution preparation for electrode fabrication, showing its potential for

development of flexible, portable, and miniaturized point-of-care medical products.

■ EXPERIMENTAL SECTION

Materials. Polyacrylonitrile (PAN; M_w = 150 000), sodium sulfate ($NaSO_4$), cobalt sulfate heptahydrate ($CoSO_4 \cdot 7H_2O$), manganese sulfate monohydrate ($MnSO_4 \cdot H_2O$), potassium chloride (KCl), potassium ferrocyanide trihydrate ($K_4Fe(CN)_6 \cdot 3H_2O$), D-fructose ($C_6H_{12}O_6$), D-lactose ($C_{12}H_{22}O_{11}$), and D-sucrose ($C_{12}H_{22}O_{11}$) were purchased from Acros Organics. Dimethylformamide (DMF), sodium hydroxide (NaOH), potassium ferricyanide ($K_3Fe(CN)_6$), glucose ($C_6H_{12}O_6$), dopamine (DA), L-ascorbic acid (AA), and uric acid (UA) were obtained from Sigma-Aldrich. Nitric acid (HNO_3) was purchased from Beaker Analyzed (69.0−70%, A.C.S. Reagent). Conductive carbon glue was obtained from Ted Pella, INC. All chemicals were of analytical reagent grade and used without further purification.

Fabrication of WA-ECNFs. The preparation of WA-ECNFs was according to our previously reported method and process.[21,27,32,40] Briefly, a self-designed sample collector consisting of four steel poles was welded on a plate to collect the ECNFs without any substrates. Then, 10 wt % PAN mixed in DMF solution was electrospun onto a fast-rolling collector at the rate of 2000 revolutions per minute (rpm) to form the well-aligned precursors. A high positive voltage of 18 kV was applied between the syringe needle and the collector, which are located 15 cm apart. The well-aligned sheets of the PAN precursor were provided at the rate of 1 mL h^{-1} for 5 h using a syringe pump. The electrospun PAN precursor was stabilized at the heat rate of 1 °C min^{-1} to 280 °C and kept for 6 h in air. Later, the stabilized sheet was carbonized at a ramping rate of 5 °C min^{-1} up to 1200 °C for 1 h in a nitrogen atmosphere to yield high-mechanical-strength ECNFs. The pristine WA-ECNFs could be obtained through these heat treatments.

Coelectrodeposition of Binary MnO_2/Co_3O_4 onto WA-ECNFs. The WA-ECNFs cut into 1.5 × 1 cm^2 were used to electrodeposit MnO_2 and Co_3O_4 with a three-electrode setup, employed a charging current of 60 μA for 3 h, and performed on a Bio-Logic VMP3 electrochemical workstation. We chose 60 μA for electrodeposition because a higher ratio of Co:Mn was obtained compared to other deposition currents (e.g., 40 μA). Here, a gold electrode decorated with ECNFs, a platinum wire, and Ag/AgCl (3 M KCl) were utilized as the working electrode, counter electrode, and reference electrode, respectively. To facilitate deposition of binary MnO_2/Co_3O_4, the WA-ECNFs were pretreated with 4 M HNO_3 at 60 °C for 3 h to introduce carboxyl and hydroxyl functional groups and to increase more active site areas for nucleation of metal oxides. The supporting electrolyte solution for electrodeposition was composed of 100 mM $NaSO_4$, 10 mM $MnSO_4$, and 20 mM $CoSO_4$. After the deposition, the obtained MnO_2/Co_3O_4@ECNFs were washed with deionized water and dried at 80 °C for further experiments. MnO_2@ECNFs followed the same procedure as MnO_2/Co_3O_4@ECNFs, except for using an aqueous solution containing 10 mM $MnSO_4$ and 100 mM $NaSO_4$. Co_3O_4@ECNFs were synthesized using 20 mM $CoSO_4$ and 100 mM $NaSO_4$ as a supporting electrolyte for electrodeposition.

Structure and Morphology Characterization. Field-emission scanning electron microscopy (FESEM) (Carl Zeiss Auriga-BU FIB FESEM microscope) at an accelerating voltage of 5.0 kV and transmission electron microscopy (TEM) (Carl Zeiss Libra 120 PLUS) were performed to study the morphological features of the well-aligned ECNFs and metal oxides nanostructured on the surface of ECNFs (MnO_2@ECNFs, Co_3O_4@ECNFs, MnO_2/Co_3O_4@ECNFs). TEM sample preparation was carried out by dissolving fibers in ethanol/water (1:1 v/v) with ultrasonication and then drop-casting dissolved fibers onto a TEM grid for imaging. Energy-dispersive X-ray spectroscopy (EDX) (Hitachi S-4800-I FESEM w/ backscattered detector and EDX) was used to obtain the elemental mapping and atomic ratio. The phase and crystalline structure of the synthesized materials were assessed by X-ray powder diffraction (XRD) (Agilent Technologies Oxford Gemini X-Ray diffractometer)
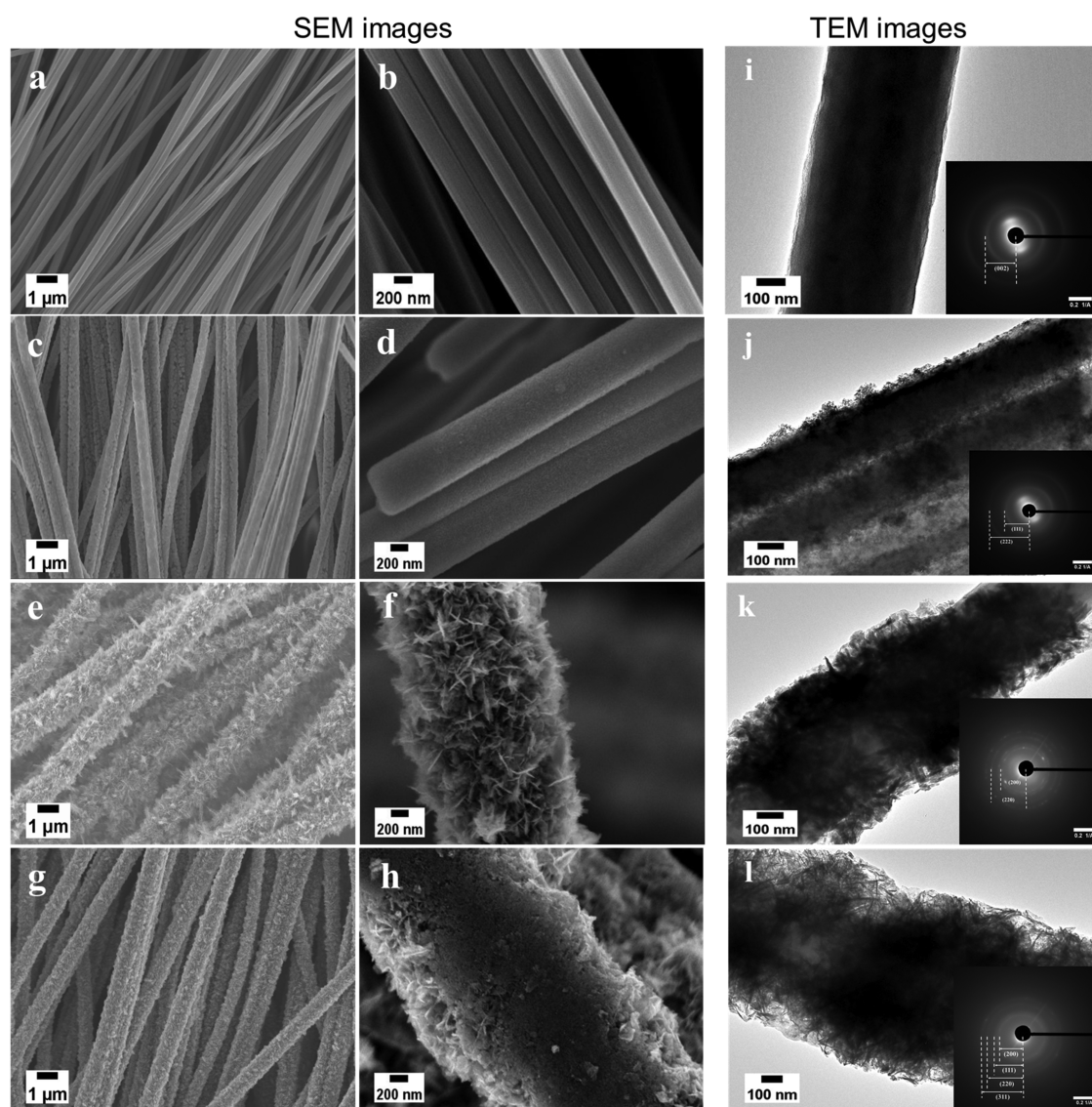
Figure 1. Low- and high-magnification SEM images of WA-ECNFs (a−b), Co_3O_4@ECNFs (c−d), MnO_2@ECNFs (e−f), and MnO_2/Co_3O_4@ECNFs (g−h) and TEM images of ECNFs (i), Co_3O_4@ECNFs (j), MnO_2@ECNFs (k), and MnO_2/Co_3O_4@ECNFs (l), respectively. The insets in (i−l) are the selected area electron diffraction (SAED).

equipped with a Cu Kα radiation source (λ = 0.15418 nm). The Raman spectrum was performed by a Horiba XploRA One Raman confocal microscope system with a 532 nm laser as the excitation source. X-ray photoelectron spectroscopy (XPS) (XPS, Thermo Fisher ESCALAB 250 Xi) was employed to study the elemental composition of the synthesized materials.

Electrochemical Measurement. All electrochemical measurements, including cyclic voltammetry (CV), Nyquist plots of electrochemical impedance spectroscopy (EIS), and chronoamperometry (CA), were performed on a bio-logic VMP3 electrochemical workstation using a three-electrode setup system with a 3 mm diameter glass carbon (GC) working electrode, a platinum wire as a counter electrode, and Ag/AgCl (3 M KCl) as a reference electrode operating at room temperature. The electrodeposited square-shaped MnO_2/Co_3O_4@ECNFs (MnO_2@ECNFs, Co_3O_4@ECNFs) were cut into wafers with geometric area 0.5 × 0.5 cm^2 and then adhered onto the GC as a modified electrode with conductive carbon glue for further electrochemical experiment. EIS was performed in 0.1 M KCl and 5 mM $[Fe(CN)_6]^{3-/4-}$ by setting the working electrode voltage at 0.0 V vs the reference electrode Ag/AgCl within the frequency range from 100 kHz to 0.01 Hz, where the distribution amplitude was 10 mV.

■ RESULTS AND DISCUSSION

Preparation of Metal Oxide Electrodes and Characterization. The morphology and structure of as-prepared ECNFs, Co_3O_4@ECNFs, MnO_2@ECNFs, and MnO_2/Co_3O_4@ECNFs were first characterized by field-emission scanning electron microscopy (FESEM) and transmission electron microscopy (TEM). Figure 1 shows the FESEM images of the pristine and modified ECNFs with metal oxides. Figure 1a,b shows low- and high-magnification FESEM images of the as-prepared pristine ECNFs. They exhibit a well-aligned and smooth surface morphology. Figure 1c−h shows the monometallic oxide or mingled binary metal oxides electrodeposited on the WA-ECNFs. As expected, the metal oxides on the scaffold were uniformly distributed to the carbon fibers. Compared to the pristine ECNFs (Figure 1a,b), the diameters of the fibers with electrodeposition of metal oxides increase significantly, resulting in successful electrodeposition of the ultimate products. Figure 1d demonstrates that Co_3O_4@WA-ECNFs possess sheetlike Co_3O_4 clusters compacted at the surfaces of the fiber scaffold. The high-magnification SEM
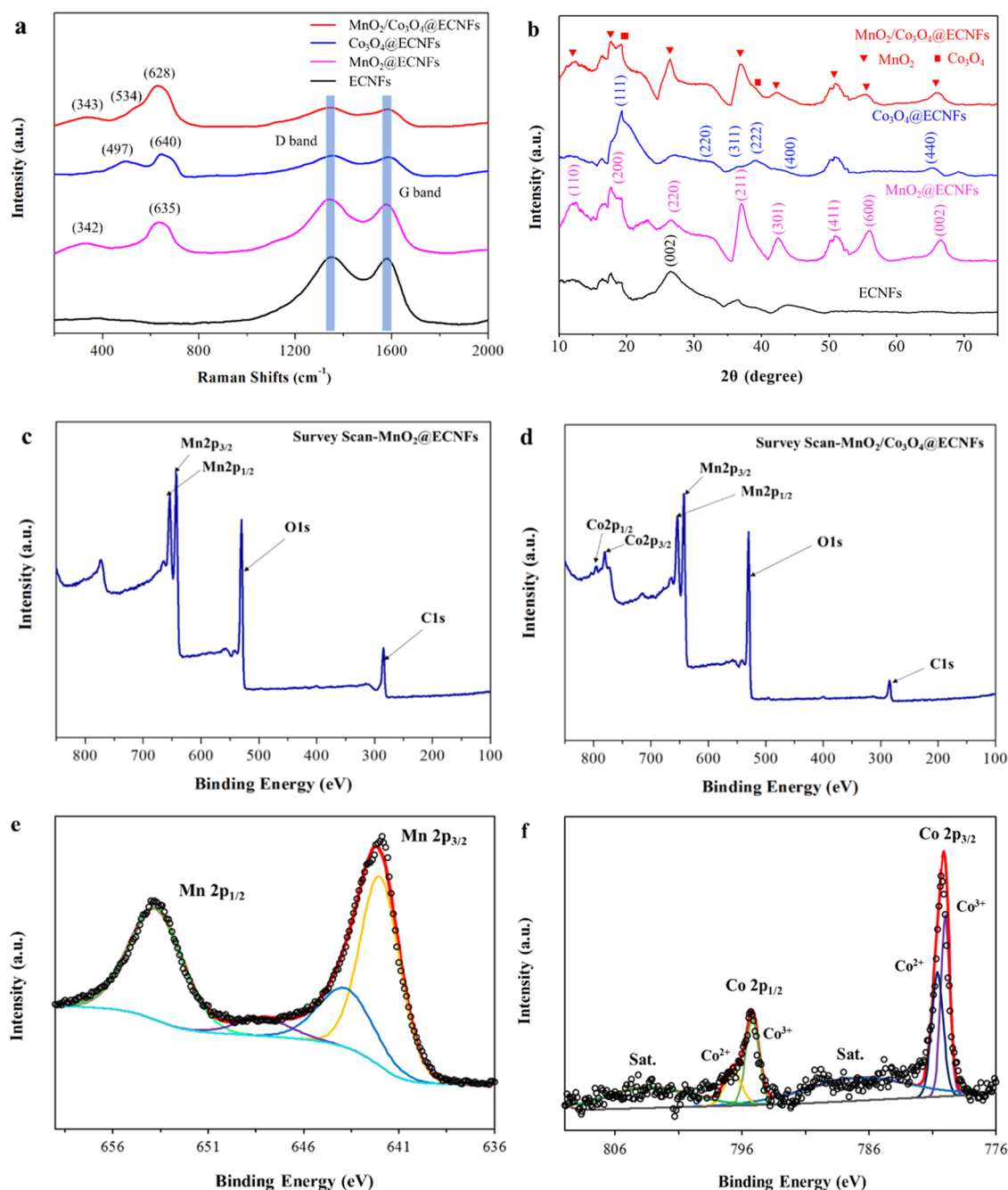
Figure 2. (a) Raman spectrum and (b) XRD patterns of the as-prepared ECNFs, MnO_2@ECNFs, Co_3O_4@ECNFs, and MnO_2/Co_3O_4@ECNFs. (c−d) Survey scan spectra of XPS of MnO_2@ECNFs and MnO_2/Co_3O_4@ECNFs, respectively. Deconvoluted peaks of (e) Mn 2p and (f) Co 2p.

image of MnO_2@WA-ECNFs (Figure 1f) shows the interconnected MnO_2 frameworks, which are composed of a mesoporous thornlike nanostructure vertically grown at the surfaces of WA-ECNFs. For the electrodeposited binary MnO_2/Co_3O_4@WA-ECNFs, the mesoporous morphology of mingled metal oxides was observed as shown in Figure 1h, which indicates the formation of hierarchical nanostructured MnO_2/Co_3O_4 hybrids. The morphology of the carbon fiber and metal oxides was further examined by TEM in Figure 1i−l, where their crystallinity was confirmed by selected area electron diffraction (SAED). The plane (002) obtained in the inset of Figure 1i is consistent with the XRD peak of ECNFs at the $2\theta = 26.54°$ plane in Figure 2b. In this pattern, the bright and broad continuous circle rings indicate the

amorphous character of carbon nanofiber layers.[41] Figure 1j shows the coated Co_3O_4 nanostructured film with compact mesopores at the carbon fiber surface where the SAED pattern represents a broad diffraction circle shape, suggesting more likely the amorphous property of Co_3O_4@WA-ECNFs. Different from Co_3O_4, the deposited MnO_2 exhibits a thornlike mesoporous structure in Figure 1k. The SAED pattern of MnO_2@WA-ECNFs is characterized by complex bright diffraction spots, which indicates that MnO_2 in the composites exists in the polycrystalline form.[42] For binary MnO_2/Co_3O_4 deposition, Figure 1l features a flocculent structure and mesopores of mingled metal oxides. Combining the amorphous structure of the Co_3O_4 film and the polycrystalline form of MnO_2, the characteristic multiconcentric diffraction
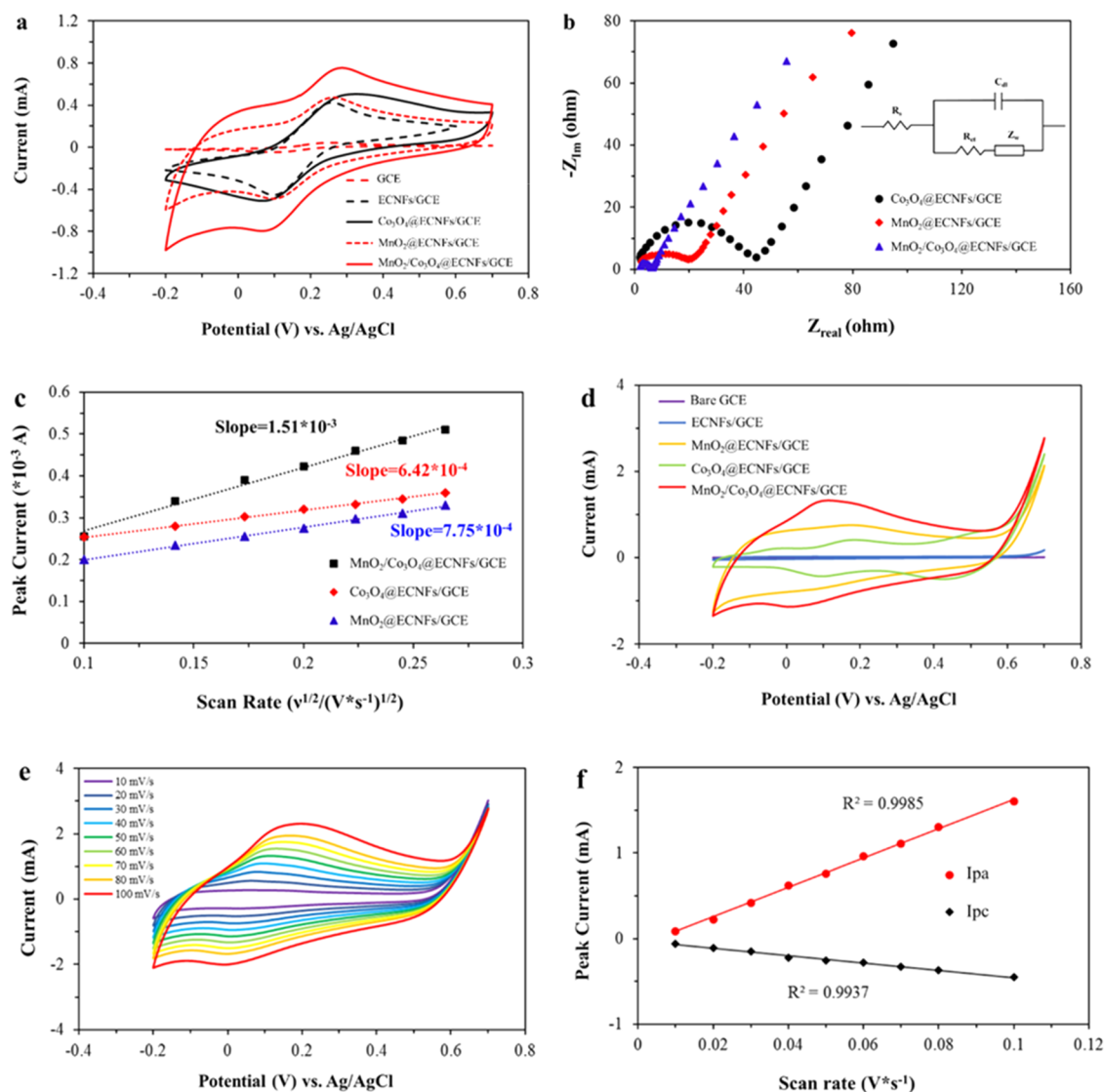
Figure 3. (a) CV curves and (b) Nyquist plots of EIS within the frequency range from 100 kHz to 0.01 Hz, where the distribution amplitude was 10 mV of different modifications of electrodes in a 0.1 M KCl solution containing 5 mM $[Fe(CN)_6]^{3-/4-}$. (c) Randles−Sevcik plots derived from the dependences of the anodic peak current on the square root of the voltage scan rate of different modified GC electrodes ($MnO_2/Co_3O_4@$ECNFs, Co_3O_4/ECNFs, MnO_2/ECNFs) immersed in a 0.6 M NaOH solution containing 5 mM $[Fe(CN)_6]^{3-}$, scan rate from 10 to 70 mV s^{-1}. (d) CV curves of different modifications of electrodes in a 0.6 M NaOH solution at the scan rate of 50 mV s^{-1}. (e) CV curves of the $MnO_2/Co_3O_4@$ECNF-modified GC electrode with different scan rates in a 0.6 M NaOH electrolyte solution. (f) Plot of peak currents vs scan rates with the $MnO_2/Co_3O_4@$ECNF-modified GC electrode.

rings of the SAED pattern in Figure 1l still show a somewhat polycrystalline nature of the nanostructured Co_3O_4/MnO_2 in the composites.

The chemical composition of $MnO_2/Co_3O_4@$ECNFs was analyzed by energy-dispersed X-ray (EDX) spectroscopy. The EDX spectra (Figure S1) verify that the surface composition of $MnO_2/Co_3O_4@$ECNFs is uniformly distributed with the elements of C, O, Mn, and Co. Therein, C and O elements are derived from the ECNFs, and the atomic ratios of manganese and cobalt are 15.82 and 1.62%, respectively, i.e., a mole ratio of ~8:1 of Mn/Co in the composite. Raman spectroscopy, a nondestructive conventional tool,[43] was used to investigate the chemical structure of the carbon materials. In Figure 2a, the Raman spectrum (black curve) of the as-prepared ECNFs shows two prominent peaks of the D-band and the G-band at Raman shifts of 1352 and 1585 cm^{-1}, corresponding to the disordered carbon and graphitic

carbon.[44] The intensity ratio of the D/G-band represents the atomic ratio of sp^3/sp^2 carbons, which is a measure of the extent of disordered graphite in plane sp^2 domains.[45] The intensity of D/G (I_D/I_G) was found to be approximately 1.03 for the as-prepared ECNFs. The Raman spectrum (Figure 2a red) of $MnO_2/Co_3O_4@$ECNFs also has both D and G bands at the same Raman shift; however, the intensity decreased significantly, ascribed to the decorated metal oxides.[46] The intensity of D and G bands for $Co_3O_4@$ECNFs and $MnO_2/Co_3O_4@$ECNFs is much less than that of ECNFs or $MnO_2@$ECNFs. This is mostly ascribed to the much more denser metal oxide parcel at the fiber surfaces. Besides, the ratio of I_D/I_G slightly decreased from 1.03 of the pristine ECNFs to 1.00 of the $MnO_2/Co_3O_4@$ECNFs. The change in the intensity ratio of D/G suggests that the increase in the graphitic degree was caused by the binding of carbon and MnO_2/Co_3O_4.[47] Moreover, the decrease in the sp^2 domains results in a defect in

the carbon matrix due to the removal of oxygen-containing groups from the ECNF surfaces.[48] For MnO$_2$@ECNFs, the Mn−O stretching vibration band present at the expected Raman shift of 635 cm^{-1}, and another peak at 342 cm^{-1}, could be regarded as the lattice vibration of Mn−O (Figure 2a magenta).[49,50] Notably, both monometallic MnO$_2$ and binary decorated ECNFs exhibit these characteristics. Besides, the characteristic Co−O Raman shifts of 497 and 640 cm^{-1} (Figure 2a blue) exist for the Co$_3$O$_4$@ECNF sample.[27] The Raman spectrum of MnO$_2$/Co$_3$O$_4$@ECNFs represents coupling of the Raman shift of the mingled binary metal oxide nanostructures co-wrapped at the surfaces of WA-ECNFs. Compared with the other two samples, MnO$_2$/Co$_3$O$_4$@ECNFs showed a slight red shift at the Raman shift of 628 cm^{-1}, which sheds light on the influence from the synergistic effect of manganese and cobalt oxides.[51] The observed Raman shift to lower wavelengths could be attributed to an increase in the crystal size of the mingled oxides based on a phonon quantum confinement model.[52]

Furthermore, the phase compositions and crystallographic structures of ECNFs, Co$_3$O$_4$@ECNFs, MnO$_2$@ECNFs, and MnO$_2$/Co$_3$O$_4$@ECNFs were examined by X-ray diffraction (XRD) measurement. In Figure 2b (black), the broad peak at around $2\theta = 26.54°$ corresponds to the (002) reflection of a graphitic-type lattice of the ECNFs. The XRD pattern of MnO$_2$@ECNFs (Figure 2b magenta) can be indexed into a pure tetragonal phase of α-MnO$_2$ (JCPDS 44-0141),[53−55] at 2θ of 12.4, 17.7, 26.6, 37.1, 42.4, 50.7, 55.9, and 66.5°, corresponding to the diffraction planes of (110), (200), (220), (211), (301), (411), (600), and (002) of MnO$_2$ crystals. The XRD spectrum (Figure 2b blue) of Co$_3$O$_4$@ECNFs matches well with the standard pattern (JCPDS No. 43-1003),[56,57] as revealed by the diffraction peaks at 2θ values of 19.18, 31.23, 36.85, 38.99, 44.72, and 64.40°, corresponding to (111), (220), (311), (222), (400), and (440) crystal planes. From the XRD spectrum of Co$_3$O$_4$@ECNFs, it is observed that all of the peaks are weak and broad, except the (111) crystal planes. Thus, the sample has poor crystallinity, which corresponds to the amorphous structure confirmed by SAED (Figure 1j). For MnO$_2$/Co$_3$O$_4$@ECNFs (Figure 2b red), the diffraction peaks at 19.2 and 39.1° can be indexed to the (111) and (222) planes of Co$_3$O$_4$,[58] respectively. The peaks of Co$_3$O$_4$ in the composite show an obvious low intensity, which can be ascribed to the small crystallite size of the distributed Co$_3$O$_4$ compared to α-MnO$_2$,[26,59] and a low atomic ratio of cobalt, which is consistent with the results of EDX spectroscopy.

The chemical composition and the metal oxidation states of the synthesized materials were further investigated using X-ray photoelectron spectroscopy (XPS). The XPS full-survey spectrum of MnO$_2$@ECNFs (Figure 2c) illustrates the presence of carbon, oxygen, and manganese on the surface of the materials by their distinctive peaks, while the survey spectrum of the hybrid MnO$_2$/Co$_3$O$_4$@ECNFs shows distinctive peaks, which could be indexed into Co$_{2p}$, Mn$_{2p}$, O$_{1s}$, and C$_{1s}$ regions (Figure 2d). The atomic ratio of cobalt obtained from the XPS result is about 1.98%, which is reasonably consistent with EDX spectroscopy (Figure S1). The high-resolution Mn$_{2p}$ spectrum (Figure 2e) of MnO$_2$/Co$_3$O$_4$@ECNFs shows two distinct peaks having a spin-energy separation of 11.4 eV at binding energies of 642.2 and 653.6 eV in the Mn 2p spectrum, signifying Mn 2p$_{3/2}$ and Mn 2p$_{1/2}$, which demonstrate the valence value of Mn^{4+} in the composite, a good agreement with the reported value of MnO$_2$.[60]

Similarly, the devolution of the complex Co$_{2p}$ spectrum in Figure 2f shows the presence of two chemically distinct states of Co^{2+} and Co^{3+}. Specially, two distinctive peaks located at 780.1 and 795.3 eV having a spin−orbital splitting of 15.2 eV can be assigned to Co 2p$_{3/2}$ and Co 2p$_{1/2}$, respectively.[61] In particular, the two principal peaks are fitted into four subpeaks, wherein the two peaks at 779.9 and 795.1 eV with the satellite peak at 786.9 eV prove the chemical nature of Co^{3+}, and the fitting peaks at 780.6 and 796.7 eV with the satellite peak at 803.4 eV are indexed to Co^{2+}.[11,62] These results verify the presence of the Co$_3$O$_4$ phase in the as-fabricated MnO$_2$/Co$_3$O$_4$@ECNFs. The O$_{1s}$ spectrum (Figure S2) is composed of three peaks at 529.6, 530.8, and 532.4 eV, which are attributed to oxygen states in the Co$_3$O$_4$ and MnO$_2$ crystal lattice, the O$_x^-$ (O$^-$ or O$_2^-$) ion absorbed by the oxygen-deficient region of the hybrid nanomaterial lattice, and additional physically absorbed and/or chemisorbed oxygen caused by the surface hydroxyl.[26,63] These functional groups will be beneficial to the electrocatalytical performance, owing to improving the wettability between the electrode and electrolyte.

Electrochemical Characterization of Metal Oxide Electrodes. The electrochemical behaviors of the as-prepared ECNF-, Co$_3$O$_4$@ECNF-, MnO$_2$@ECNF-, or MnO$_2$/Co$_3$O$_4$@ ECNF-modified GC electrodes and bare GCE in 0.1 M KCl containing 5 mM [Fe(CN)$_6$]$^{3-/4-}$ were first studied at a scan rate of 20 mV/s by cyclic voltammetry (Figure 3a). The cyclic voltammograms (CVs) of bare GCE present a pair of anodic and cathodic peaks with a lower peak current signal than those of electrodes with different modified ECNFs. Besides, the current values represent the sum of the charge current in the positive and negative scan directions at the modified electrodes, correspondingly. Herein, the geometric area could be used for qualitative determination of charge capacitance. Therefore, the electrode decorated with MnO$_2$/Co$_3$O$_4$@ ECNFs exhibits the highest charge current storage ability over the others, as shown in Figure 3a.

Electrochemical impedance spectroscopy (EIS) was carried out to investigate the electrochemical kinetics of GC electrodes modified with different metal oxide electrocatalysts. Figure 3b exhibits the EIS spectra of three electrodes, i.e., Co$_3$O$_4$@ ECNFs, MnO$_2$@ECNFs, and MnO$_2$/Co$_3$O$_4$@ECNFs. Efficient charge-transport ability was confirmed by the Nyquist plots in Figure 3b, whose data were analyzed by fitting a Randle equivalent circuit,[64] as shown in the inset. The Nyquist plot consists of a depressed overlapping capacitive semicircle in the high-frequency region and a linear line in the low-frequency domain. The diameter of the semicircle in the high frequency indicates the bulk charge-transfer resistance (R_{ct}), while the linear portion is attributed to an interfacial diffusion-limited process.[65] Therein, MnO$_2$/Co$_3$O$_4$@ECNFs show the smallest semicircle and the lowest R_{ct} (~8 Ω) compared to the ones that electrodeposited monometallic oxide of MnO$_2$ (~20 Ω) or Co$_3$O$_4$ (~45 Ω) onto the WA-ECNFs, indicating the highest efficient electron and mass transport at the MnO$_2$/ Co$_3$O$_4$@ECNF electrode. The decrease in resistance could be ascribed to the porous structure with a more accessible surface area for the electrolyte ions.[66] This corroborates the improvement of ion diffusion to the electrode surface and electrical conductivity due to the structural and morphological features of the binary MnO$_2$/Co$_3$O$_4$@ECNFs.
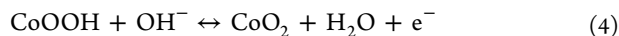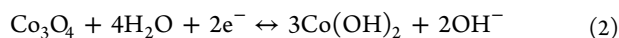
To assess the specific active surface area of the modified GC electrode in electrochemistry, CV curves were recorded at

different scan rates in a 0.6 M NaOH solution containing 5 mM $[Fe(CN)_6]^{3-}$ (Figure S3). The peak current for the reversible redox reaction is given by the Randles−Sevcik equation[67]

$$I_p = 2.69 \times 10^5 n^{3/2} A C_0 D^{1/2} \nu^{1/2} \tag{1}$$

where n represents the number of electrons, A represents the active surface area of the electrode (in cm^2), C_0 is the concentration of the electroactive compounds (in $mol\ cm^{-3}$), D is the diffusion coefficient of $[Fe(CN)_6]^{3-}$ ($7.6 \times 10^{-6}\ cm^2\ s^{-1}$),[47] and ν represents the scan rate (in $V\ s^{-1}$). The active surface area was determined by the slope of the linear behavior of I_p vs $\nu^{1/2}$ (Figure 3c). The active surface area of different modified electrodes was obtained as $0.41 \pm 0.01\ cm^2$ for MnO_2/Co_3O_4@ECNFs, $0.17 \pm 0.01\ cm^2$ for Co_3O_4@ECNFs, and $0.20 \pm 0.01\ cm^2$ for MnO_2@ECNFs. Such findings agree with the morphology analysis by SEM and TEM images. The electrode of MnO_2/Co_3O_4@ECNFs shows the highest current signal in Figure 3a owing to its highest electron conduction property and largest specific active surface area compared to ECNFs, Co_3O_4@ECNFs, or MnO_2@ECNFs.

Figure 3d shows the steady-state CV curves of different electrodes in a 0.6 M NaOH electrolyte solution without any analyte (glucose) at a scan rate of 50 mV s⁻¹. CV experiments were carried out in the potential range from −0.2 to 0.7 V vs Ag/AgCl to observe the redox reaction of the electrodes. The anodic and cathodic peaks only can be observed on the electrodes modified with metal oxides on the WA-ECNFs. There are no noticeable redox peaks observed for either the bare GCE or ECNF-modified GCE in the alkaline solution. One can conclude that the oxidation and reduction peaks arise from the metal oxides of Co_3O_4 and/or MnO_2. In the CV curve of Co_3O_4@ECNFs/GCE (Figure 3d green curve), two pairs of redox peaks were observed at oxidation peaks, 0.15 and 0.48 V, which can be assigned to the reversible transition between Co_3O_4 and CoOOH, as well as the transition between CoOOH and CoO_2 (eqs 2−4), respectively.[26,68]

$$Co_3O_4 + 4H_2O + 2e^- \leftrightarrow 3Co(OH)_2 + 2OH^- \tag{2}$$

$$Co(OH)_2 + OH^- \leftrightarrow CoOOH + H_2O + e^- \tag{3}$$

$$CoOOH + OH^- \leftrightarrow CoO_2 + H_2O + e^- \tag{4}$$

In addition, a pair of broad but weak oxidation and reduction peaks of MnO_2@ECNFs/GCE between −0.1 and 0.4 V was obtained in Figure 3d (yellow curve), owing to the oxidation of MnO_2 to Mn (VI) and reduction of Mn (VI) to MnO_2.[69] Moreover, the binary MnO_2/Co_3O_4@ECNFs/GCE shows a high-intensity redox pair with a larger broad oxidation peak at around 0.1 V in Figure 3d (red curve). The presence of a single oxidation peak in the electrocatalytical system with two metal oxides suggests that the centers of nanocomposites act together in the electrochemical reaction. Besides, this oxidation peak potential of the binary metal oxide electrode has a shift to a smaller overpotential than that of the monometallic oxide, MnO_2 or Co_3O_4 (eqs 3 and 4) electrode, suggesting a faster kinetics of the redox reaction. Such a shift in the negative direction is attributed to the "mingled" binary metal oxides and increased interfaces, which enhance the active sites and large electron transport channels in the electrode. It is expected that molecules and ions involved in glucose oxidation will be facilitated to approach the active sites, and the activation energy, i.e., the required applied voltage, for glucose oxidation

will be reduced, thus accelerating the catalyzed reaction.[70] Furthermore, the MnO_2/Co_3O_4@ECNF electrode exhibits a much higher current and capacitance in the electrolyte solution compared to the electrode of monometallic oxide MnO_2 or Co_3O_4, a manifestation of its higher conductivity and larger specific electrochemical surface area.

To confirm the intrinsic redox reactions of metal oxides, the relationship between the peak current and voltage scan rate was determined using cyclic voltammetry in 0.6 M NaOH. The measurements were carried out under different scan rates (10, 20, 30, 40, 50, 60, 70, 80, and 100 mV/s). The results are shown in Figure 3e for the binary metal oxides and in Figure S4a,c for monometallic oxides Co_3O_4@ECNFs and MnO_2@ECNFs, respectively. The linear relationship of the anodic and cathodic peak currents vs the scan rate (Figure 3f and S4b,d) indicates that the redox reactions of the metal-oxide-decorated electrodes are a typical surface-confined reaction.[71]

Electrooxidation of Glucose at Metal Oxide Electrodes. The electrooxidation of glucose at Co_3O_4@ECNFs/GCE, MnO_2@ECNFs/GCE, and MnO_2/Co_3O_4@ECNFs/GCE was characterized by cyclic voltammetry. Figure 4a demonstrates the CVs of the binary MnO_2/Co_3O_4@ECNF electrode with glucose concentrations in the range from 0 to 7 mM. The oxidation peak currents increase correspondingly with the increase in glucose concentration, an indication of glucose oxidation. Taking the peak currents at the potential position of 0.55 V, which shows the most significant changes with the addition of glucose, we plotted the corresponding calibration curve of the peak current as a function of glucose concentration (Figure 4b). It displays a linear correlation over the glucose concentration with a correlation coefficient of 0.987. Similarly, the CV curves (Figure S5) of Co_3O_4@ECNFs and MnO_2@ECNFs were also obtained with the addition of glucose. The linear fitting of the calibration curves gives the slopes of 0.0655, 0.1986, and 0.2258 for MnO_2@ECNFs, Co_3O_4@ECNFs, and MnO_2/Co_3O_4@ECNFs, respectively. To further understand the enhanced electrochemical performance of MnO_2/Co_3O_4@ECNFs toward glucose oxidation, the Tafel curves were obtained in Figure S6, depicting a comparison for the three types of electrodes. In the Tafel curve of MnO_2/Co_3O_4@ECNFs, the equilibrium potential as defined by the zero overpotential was observed at −0.13 V. However, MnO_2@ECNFs and Co_3O_4@ECNFs possess more negative equilibrium potentials, −0.15 and −0.18 V, compared to the hybrid electrode. The hybrid MnO_2/Co_3O_4@ECNF electrode demonstrates the highest kinetics (largest exchange current density at equilibrium potential). In addition, the Tafel slope of the three electrodes followed a trend as Co_3O_4@ECNFs > MnO_2@ECNFs > MnO_2/Co_3O_4@ECNFs, shown in Figure 4c. The lowest Tafel slope of the hybrid composite electrode indicates the highest charge transferability of the materials,[72] suggesting the synergistic effect of mingled metal oxides at ECNFs. These results indicate a better electrooxidative performance of MnO_2/Co_3O_4@ECNFs than the monometallic oxide electrodes. The plausible reactions involved in the electrocatalytic oxidation of glucose at the MnO_2/Co_3O_4@ECNF electrode are described in eqs 5 and 6.[73] The CoO_2 and MnO_2 in the presence of glucose convert to CoOOH and MnOOH, respectively. Therefore, the redox reactions would greatly promote to the forward oxidative reaction (CoOOH → CoO_2, MnOOH → MnO_2), resulting in a monotonic increase of the oxidation peak upon the addition of glucose.
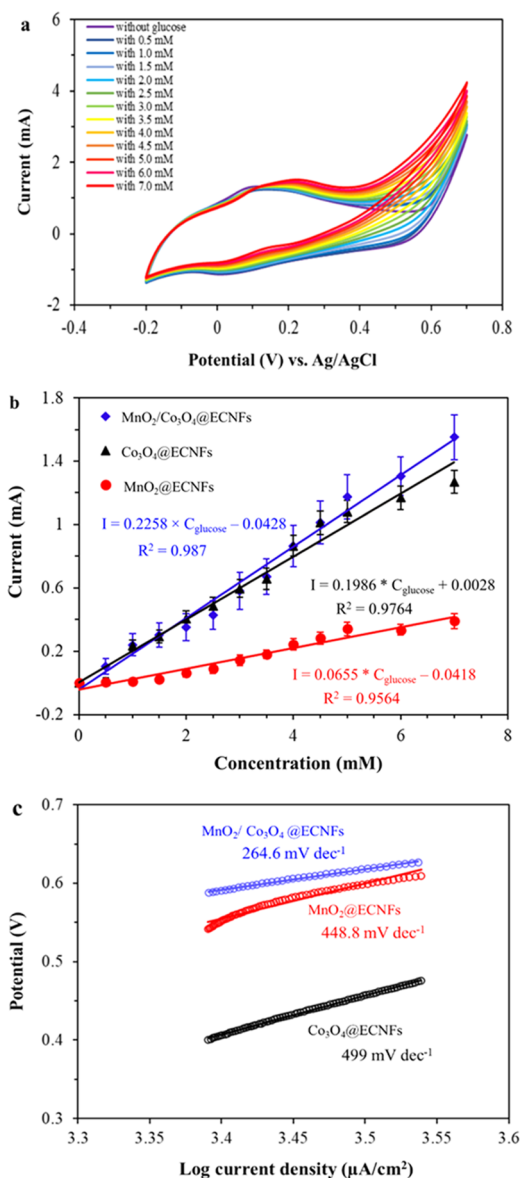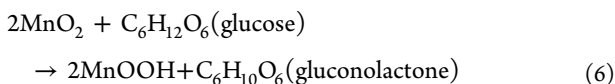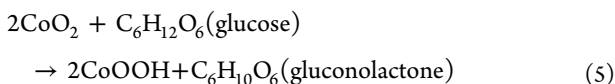
Figure 4. (a) CV curves of MnO_2/Co_3O_4@ECNFs/GCE at different concentrations of glucose, ranging from 0.5 to 7 mM at the scan rate of 50 mV/s. (b) Corresponding calibration plot of the oxidation current vs concentration of glucose of the MnO_2/Co_3O_4@ECNFs, Co_3O_4@ECNFs, and MnO_2@ECNFs. (c) Tafel slope diagram of various electrodes with 1 mM glucose.

$$2CoO_2 + C_6H_{12}O_6(glucose)$$
$$\rightarrow 2CoOOH + C_6H_{10}O_6(gluconolactone) \quad (5)$$

$$2MnO_2 + C_6H_{12}O_6(glucose)$$
$$\rightarrow 2MnOOH + C_6H_{10}O_6(gluconolactone) \quad (6)$$

According to aforementioned reaction mechanisms, the electrooxidation of glucose at the binary metal oxide electrode is schematically illustrated in Scheme 1. Because the MnO_2/Co_3O_4@ECNFs demonstrate good alignment and mesoporous morphology of metal oxides, the scaffold not only enhances the mobility of electrons through the whole body of MnO_2/Co_3O_4@ECNFs but also extends the number of electron-transfer channels. Hence, it may increase the delocalization of charges, realizing improved conductivity and better electro-

chemical performance in efficiency for glucose oxidation. The glucose molecules diffuse onto the high porosity of the binary metal oxides and then access and absorb to the metal oxide catalytic active sites, followed by electrocatalytic oxidation. Intimate contact of the heterogeneous interfaces with glucose molecules with minimal diffusion resistance is achieved.[74] Besides, such hybrid nanomaterials integrate the fine electronic configuration of the semiconductor of MnO_2 and Co_3O_4, which have more valence states to provide more redox reactions.[26,63] It is plausible that the charge transfers from the p orbital of O in the glucose molecules to the d orbital of Mn and Co in the nanocomposite enhance the density of state (DOS) of Mn and Co d-orbitals near the Fermi level after anchoring glucose molecules. The presence of occupied states near the Fermi level would be in favor of metal ions to transfer charges from the glucose through redox reactions. Hence, the synergistic effect between WA-ECNFs and binary metal oxides is expected. The MnO_2/Co_3O_4@ECNFs possess a nonzero DOS at the Fermi level, where substantial charge transfer from metal oxides to ECNFs occurs due to the energy difference in valence between conduction band edges and conductivity in the presence of ECNFs, which in turn may enhance the sensitivity of the nonenzymatic sensor from MnO_2/Co_3O_4@ ECNFs.[75]

Amperometry Detection of Glucose. Because the MnO_2/Co_3O_4@ECNF electrode shows better electrocatalytic activity in contrast to the monometallic oxide at ECNFs, it was tested for amperometric glucose sensing. Amperometry is a simple and economic electrochemical technique for evaluating sensing applications in terms of sensitivity and specificity. To determine the best voltage for the electrocatalytic reaction of glucose oxidation, we measured the current responses in the presence of glucose at different voltages. Figure S7 displays the results, which clearly indicate that the potential at 0.55 V has the greatest electrocatalytic current of glucose oxidation for optimal electrochemical sensitivity and selectivity.

The real-time amperometric detection of glucose using the MnO_2/Co_3O_4@ECNF electrode was performed by the successive stepwise addition of different concentrations of glucose into a stirring alkaline electrolyte solution at fixed intervals at an applied potential of 0.55 V, resulting in a steep rise in the current (Figure 5a). The nonenzymatic electrode demonstrated a rapid glucose response at a concentration of 5 μM by reaching a steady signal within 5 s. The limit of detection (LOD) was determined to be 0.3 μM (with $S/N = 3$) and the detection sensitivity was 1159 μA mM^{-1} cm^{-2}, as determined by the slope of the linear fitting. The detection performance of this enzymeless glucose sensor was compared to a series of reported enzymeless glucose sensings based on MnO_2 or Co_3O_4, as shown in Table S1. The MnO_2/Co_3O_4@ ECNF electrode in this work exhibits greatly improved sensitivity and detection limit in comparison to most reported results.

Figure 5b shows that the corresponding calibration curve fits well with a Langmuir isothermal model. This result suggests that the electrochemical oxidation of glucose on MnO_2/Co_3O_4@ECNFs is a surface catalytic reaction.[61] The calibration data fit the Langmuir isothermal equation very well over a range of concentrations from 5 μM to 10.9 mM ($R^2 = 0.9997$), which is expressed as eq 7

Scheme 1. Schematic Illustration of the Proposed Electrocatalytic Mechanisms for Glucose Oxidation at the $MnO_2/Co_3O_4@$ ECNF Hybrid Structure

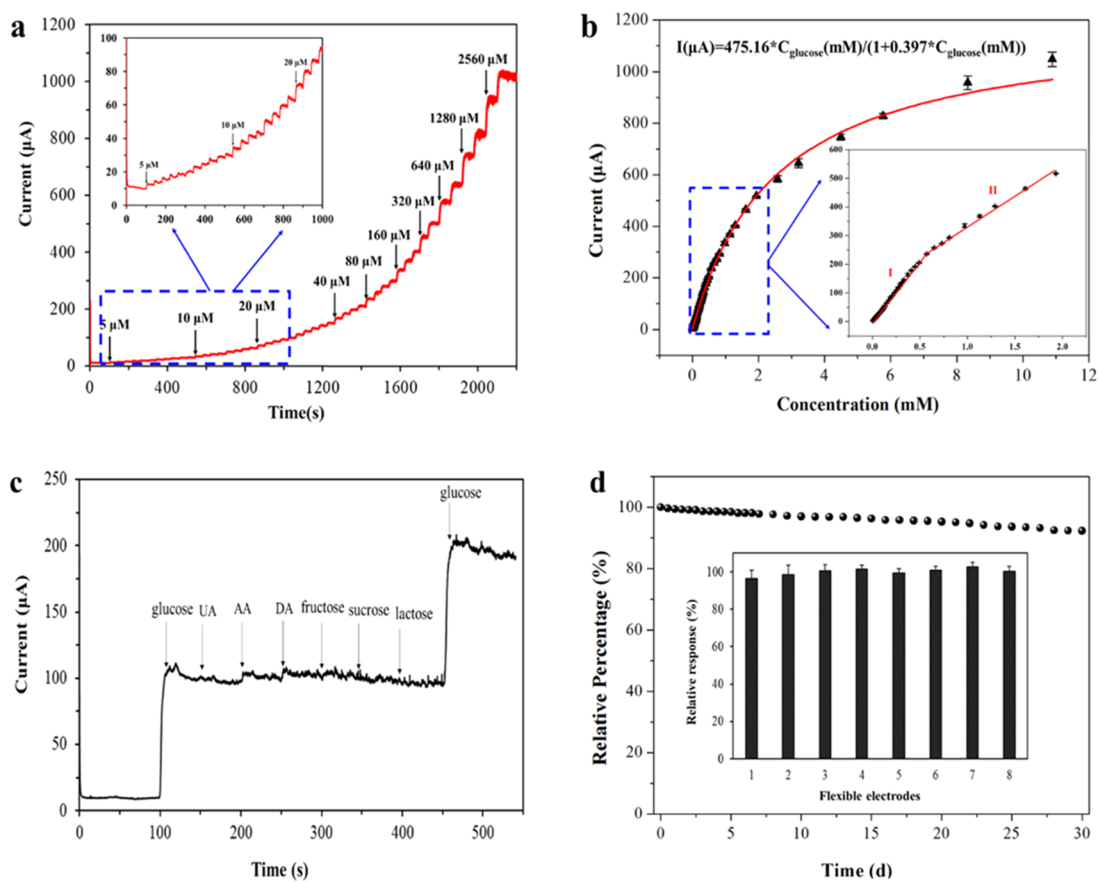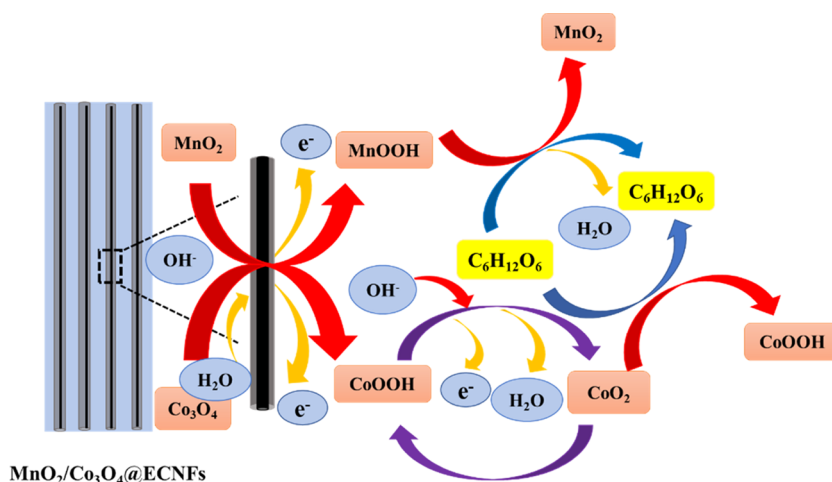**Figure 5.** a Typical amperometric response of the GC electrode modified with $MnO_2/Co_3O_4@ECNFs$ against successive additions of different glucose concentrations in 0.6 M NaOH at a constant applied potential of 0.55 V (v. Ag/AgCl). (b) Corresponding Langmuir isothermal fitting curve (red line); the inset is a zoom of the linear range. (c) Amperometric response of $MnO_2/Co_3O_4@ECNFs/GCE$ to the addition of glucose (0.25 mM) and different inferences (0.025 mM, respectively) in 0.6 M NaOH at an applied potential of 0.55 V (v. Ag/AgCl). (d) Variation of the response current of the $MnO_2/Co_3O_4@ECNF$-based nonenzymatic glucose sensor to 5.0 mM glucose with time, and the inset is the current response of eight separately prepared $MnO_2/Co_3O_4@ECNFs/GC$ electrodes to 5.0 mM glucose.

$$I(\mu A) = 475.16 \times C_{glucose}(mM)$$

$$/(1 + 0.397 \times C_{glucose}(mM)) \qquad (7)$$

When the glucose concentration is as low as $0.397 \times C_{glucose} \ll 1$, eq 7 can be approximated as a linear equation: $I(\mu A) =$

$475.16 \times C_{glucose}$ (mM). In this case, sensitivity is calculated to be 1159 μA mM^{-1} cm^{-2}, which reasonably agrees with the experimental result (1045 μA mM^{-1} cm^{-2}) if only considering the linear range of 5 μM–0.57 mM. On the other hand, glucose oxidation can be separated into two ranges of linear functions for the concentration of 5 μM–0.57 mM and 0.57

mM−1.93 mM (inset: Figure 5b). The two linear calibration plots of oxidation current vs glucose concentration can be fitted as follows: (I) $I(\mu A) = 428.52 \times C_{glucose} - 0.2016$ ($R^2 = 0.9985$); and (II): $I(\mu A) = 209.42 \times C_{glucose} + 124.23$ ($R^2 = 0.9948$). The sensitivity of the concentration range of 0.57−1.93 mM is calculated to be 511 μA mM^{-1} cm^{-2}. The fit of the Langmuir isothermal theory to the electrooxidation of glucose suggests that the reaction is limited by the absorption process of glucose onto the electrochemically active sites followed by a fast redox reaction and charge transfer. In the linear range of 5 μM−0.57 mM of the fit, MnO$_2$/Co$_3$O$_4$@ECNFs could ideally both absorb the glucose molecules and desorb the reaction of byproducts efficiently to allow further catalytic reactions to take place. When $C_{glucose}$ further increases to the range of 0.57−1.93 mM, the MnO$_2$ and Co$_3$O$_4$ in the hybrid nanoelectrode allow them to strongly bind to the glucose molecules via van der Waals interactions because of the formation of a band between O of glucose and O of the hybrid MnO$_2$/Co$_3$O$_4$, accompanied by a large change in the density of states (DOS), where the glucose molecules are at the valence band maximum of the hybrids.[75] At higher concentrations, it is unlikely that the glucose molecules can be oxidized and then released from the defect for efficient sensing because of surface fouling from byproducts of glucose oxidation, thus decreasing the diffusion coefficient and slowing down the electron transfer.[76]

The specificity of the MnO$_2$/Co$_3$O$_4$@ECNFs/GC electrode is a significant parameter to evaluate the performance of an electrochemical glucose sensor. Some endogenous compounds, such as uric acid (UA), ascorbic acid (AA), dopamine (DA), fructose, sucrose, and lactose, typically coexist with glucose in physiological fluids. The physiological glucose level is normally 10 times higher than the interferences. Hence, the MnO$_2$/Co$_3$O$_4$@ECNFs/GC electrode was evaluated using those compounds. Figure 5c shows the amperometric responses with glucose and interfering substances at the applied voltage of 0.55 V vs Ag/AgCl. It was observed that the addition of other carbohydrate isomers had a negligible influence on glucose electrochemical signals at the MnO$_2$/Co$_3$O$_4$@ECNF electrode, indicating that the resultant amperometric sensor is highly selective for the detection of glucose.

Furthermore, the stability of the MnO$_2$/Co$_3$O$_4$@ECNF electrode stored at room temperature was investigated by periodically recording its current response to 5.0 mM glucose. The oxidation current retained 92.3% of its initial value after 30 days (Figure 5d). Besides, the reproducibility of the glucose sensor was evaluated independently at a given glucose concentration for five successive measurements with eight different MnO$_2$/Co$_3$O$_4$@ECNFs/GC electrodes. The results provide a relative standard deviation less than 4% (Figure 5d inset), confirming that the binary metal oxide electrodes have great long-term stability and reproducibility. The practical testing of this MnO$_2$/Co$_3$O$_4$@ECNF electrode was established by spiking human serum samples with a predetermined amount of glucose solution. The human serum was centrifuged at 10 000 rmp for 15 min and diluted 50 times with (1×) potassium buffer solution (PBS) at pH 7.4. Then, the diluted serum was mixed with different concentrations of glucose and added into the experimental system. The measurement results are summarized in Table S2. The recovery rates of the spiked standard solutions are almost 100%, indicating the potential of the nonenzymatic glucose sensor in practical applications.

CONCLUSIONS

In summary, an electrode of binary metal oxides (MnO$_2$/Co$_3$O$_4$) decorated on the WA-ECNFs has been successfully synthesized through a facile electrodeposition technique. The MnO$_2$/Co$_3$O$_4$ metal oxides exhibit mesoporous surfaces with excellent electrochemical performance for glucose sensing. Primarily, the morphology of the binary metal oxides guarantees improved electrical conductivity (faster charge transfer), increased active surface area in electrochemistry over the monometallic oxides (MnO$_2$ or Co$_3$O$_4$), and facilitated mass transfer to the surfaces. The defects in the hybrid nanoelectrode have more valence states to provide redox reactions and allow an electronic configuration to facilitate charge transfer. These synergistic effects of binary metal oxides with an aligned scaffold significantly improved the sensing activity with an excellent sensitivity of 1159 μA mM^{-1} cm^{-2} and a good detection limit of 0.3 μM ($S/N = 3$) with a dynamic range from 5 μM to 10.9 mM. The nonenzymatic glucose biosensor was tested with high specificity, long-term stability, and reproducibility. It shows almost 100% recovery for detection of glucose spiked in human serum samples. This work demonstrates significant improvement in developing metal-oxide-based, low-cost, and highly efficient nonenzymatic electrooxidation of glucose and an electrochemical sensor detection.

ASSOCIATED CONTENT

ⓢ Supporting Information

The Supporting Information is available free of charge at https://pubs.acs.org/doi/10.1021/acs.cgd.0c01299.

EDX data, additional XPS spectrum, electrochemical data, comparison table for state-of-the art detection, and data table for serum glucose detection (PDF)

AUTHOR INFORMATION

Corresponding Authors

Xinping Zeng − *Department of Nanoscience, Joint School of Nanoscience and Nanoengineering, University of North Carolina at Greensboro, Greensboro, North Carolina 27401, United States; School of Life Sciences and Technology, Tongji University, Shanghai 200092, P. R. China*; Email: zengxp@tongji.edu.cn

Jianjun Wei − *Department of Nanoscience, Joint School of Nanoscience and Nanoengineering, University of North Carolina at Greensboro, Greensboro, North Carolina 27401, United States;* ⓞ orcid.org/0000-0002-2658-0248; Email: j_wei@uncg.edu

Authors

Ziyu Yin − *Department of Nanoscience, Joint School of Nanoscience and Nanoengineering, University of North Carolina at Greensboro, Greensboro, North Carolina 27401, United States*

Kokougan Allado − *Department of Nanoscience, Joint School of Nanoscience and Nanoengineering, University of North Carolina at Greensboro, Greensboro, North Carolina 27401, United States*

Alex T. Sheardy − *Department of Nanoscience, Joint School of Nanoscience and Nanoengineering, University of North Carolina at Greensboro, Greensboro, North Carolina 27401, United States*

Zuowei Ji − *Department of Nanoscience, Joint School of Nanoscience and Nanoengineering, University of North Carolina at Greensboro, Greensboro, North Carolina 27401, United States*

Durga Arvapalli − *Department of Nanoscience, Joint School of Nanoscience and Nanoengineering, University of North Carolina at Greensboro, Greensboro, North Carolina 27401, United States*

Mengxin Liu − *Department of Nanoscience, Joint School of Nanoscience and Nanoengineering, University of North Carolina at Greensboro, Greensboro, North Carolina 27401, United States*

Peng He − *Department of Chemistry, North Carolina Agricultural and Technical State University, Greensboro, North Carolina 27411, United States;* ⊙ orcid.org/0000-0002-4773-7566

Complete contact information is available at:
https://pubs.acs.org/10.1021/acs.cgd.0c01299

◼ REFERENCES

(1) Lee, S.; Lee, J.; Park, S.; Boo, H.; Kim, H. C.; Chung, T. D. Disposable non-enzymatic blood glucose sensing strip based on nanoporous platinum particles. *Appl. Mater. Today* **2018**, *10*, 24−29.

(2) Xu, J.; Li, F.; Wang, D.; Nawaz, M. H.; An, Q.; Han, D.; Niu, L. Co_3O_4 nanostructures on flexible carbon cloth for crystal plane effect of nonenzymatic electrocatalysis for glucose. *Biosens. Bioelectron.* **2019**, *123*, 25−29.

(3) Gao, H.; Xiao, F.; Ching, C. B.; Duan, H. One-step electrochemical synthesis of PtNi nanoparticle-graphene nanocomposites for nonenzymatic amperometric glucose detection. *ACS Appl. Mater. Interfaces* **2011**, *3*, 3049−3057.

(4) Dong, Q.; Wang, X.; Willis, W. S.; Song, D.; Huang, Y.; Zhao, J.; Li, B.; Lei, Y. Nitrogen-doped Hollow Co_3O_4 Nanofibers for both Solid-state pH Sensing and Improved Non-enzymatic Glucose Sensing. *Electroanalysis* **2019**, *31*, 678−687.

(5) Zhu, H.; Li, L.; Zhou, W.; Shao, Z.; Chen, X. Advances in non-enzymatic glucose sensors based on metal oxides. *J. Mater. Chem. B* **2016**, *4*, 7333−7349.

(6) Zhi, M.; Xiang, C.; Li, J.; Li, M.; Wu, N. Nanostructured carbon−metal oxide composite electrodes for supercapacitors: a review. *Nanoscale* **2013**, *5*, 72−88.

(7) Zhang, Z.; Liu, J.; Gu, J.; Su, L.; Cheng, L. An overview of metal oxide materials as electrocatalysts and supports for polymer electrolyte fuel cells. *Energy Environ. Sci.* **2014**, *7*, 2535−2558.

(8) Li, L.; Scott, K.; Yu, E. H. A direct glucose alkaline fuel cell using MnO_2−carbon nanocomposite supported gold catalyst for anode glucose oxidation. *J. Power Sources* **2013**, *221*, 1−5.

(9) Guo, C.; Li, H.; Zhang, X.; Huo, H.; Xu, C. 3D porous CNT/MnO_2 composite electrode for high-performance enzymeless glucose detection and supercapacitor application. *Sens. Actuators, B* **2015**, *206*, 407−414.

(10) Ponnusamy, R.; Venkatesan, R.; Kandasamy, M.; Chakraborty, B.; Rout, C. S. MnO_2 polymorph selection for non-enzymatic glucose detection: An integrated experimental and density functional theory investigation. *Appl. Surf. Sci.* **2019**, *487*, 1033−1042.

(11) Liu, L.; Jiang, Z.; Fang, L.; Xu, H.; Zhang, H.; Gu, X.; Wang, Y. Probing the crystal plane effect of Co_3O_4 for enhanced electrocatalytic performance toward efficient overall water splitting. *ACS Appl. Mater. Interfaces* **2017**, *9*, 27736−27744.

(12) Li, Y.; Zhang, L.; Peng, J.; Zhang, W.; Peng, K. Magnetic field enhancing electrocatalysis of Co_3O_4/NF for oxygen evolution reaction. *J. Power Sources* **2019**, *433*, No. 226704.

(13) Dong, X.-C.; Xu, H.; Wang, X.-W.; Huang, Y.-X.; Chan-Park, M. B.; Zhang, H.; Wang, L.-H.; Huang, W.; Chen, P. 3D graphene−cobalt oxide electrode for high-performance supercapacitor and enzymeless glucose detection. *ACS Nano* **2012**, *6*, 3206−3213.

(14) Yuan, B.; Xu, C.; Deng, D.; Xing, Y.; Liu, L.; Pang, H.; Zhang, D. Graphene oxide/nickel oxide modified glassy carbon electrode for supercapacitor and nonenzymatic glucose sensor. *Electrochim. Acta* **2013**, *88*, 708−712.

(15) Ci, S.; Huang, T.; Wen, Z.; Cui, S.; Mao, S.; Steeber, D. A.; Chen, J. Nickel oxide hollow microsphere for non-enzyme glucose detection. *Biosens. Bioelectron.* **2014**, *54*, 251−257.

(16) Ahmad, R.; Vaseem, M.; Tripathy, N.; Hahn, Y.-B. Wide linear-range detecting nonenzymatic glucose biosensor based on CuO nanoparticles inkjet-printed on electrodes. *Anal. Chem.* **2013**, *85*, 10448−10454.

(17) Song, J.; Xu, L.; Zhou, C.; Xing, R.; Dai, Q.; Liu, D.; Song, H. Synthesis of graphene oxide based CuO nanoparticles composite electrode for highly enhanced nonenzymatic glucose detection. *ACS Appl. Mater. Interfaces* **2013**, *5*, 12928−12934.

(18) Meng, F.; Shi, W.; Sun, Y.; Zhu, X.; Wu, G.; Ruan, C.; Liu, X.; Ge, D. Nonenzymatic biosensor based on Cu_xO nanoparticles deposited on polypyrrole nanowires for improving detectionrange. *Biosens. Bioelectron.* **2013**, *42*, 141−147.

(19) Wen, Q.; Wang, S.; Yan, J.; Cong, L.; Pan, Z.; Ren, Y.; Fan, Z. MnO_2−graphene hybrid as an alternative cathodic catalyst to platinum in microbial fuel cells. *J. Power Sources* **2012**, *216*, 187−191.

(20) Du, G.; Liu, X.; Zong, Y.; Hor, T. A.; Yu, A.; Liu, Z. Co_3O_4 nanoparticle-modified MnO_2 nanotube bifunctional oxygen cathode catalysts for rechargeable zinc−air batteries. *Nanoscale* **2013**, *5*, 4657−4661.

(21) Zeng, Z.; Zhang, W.; Liu, Y.; Lu, P.; Wei, J. Uniformly electrodeposited α-MnO_2 film on super-aligned electrospun carbon nanofibers for a bifunctional catalyst design in oxygen reduction reaction. *Electrochim. Acta* **2017**, *256*, 232−240.

(22) Wang, H.-Y.; Hung, S.-F.; Chen, H.-Y.; Chan, T.-S.; Chen, H. M.; Liu, B. In operando identification of geometrical-site-dependent water oxidation activity of spinel Co_3O_4. *J. Am. Chem. Soc.* **2016**, *138*, 36−39.

(23) Du, S.; Ren, Z.; Zhang, J.; Wu, J.; Xi, W.; Zhu, J.; Fu, H. Co_3O_4 nanocrystal ink printed on carbon fiber paper as a large-area electrode for electrochemical water splitting. *Chem. Commun.* **2015**, *51*, 8066−8069.

(24) Chang, T.; Shen, Z.; Huang, Y.; Lu, J.; Ren, D.; Sun, J.; Cao, J.; Liu, H. Post-plasma-catalytic removal of toluene using MnO_2−Co_3O_4 catalysts and their synergistic mechanism. *Chem. Eng. J.* **2018**, *348*, 15−25.

(25) Li, X.; Sun, Y.; Wu, Q.; Liu, H.; Gu, W.; Wang, X.; Cheng, Z.; Fu, Z.; Lu, Y. Optimized electronic configuration to improve the surface absorption and bulk conductivity for enhanced oxygen evolution reaction. *J. Am. Chem. Soc.* **2019**, *141*, 3121−3128.

(26) Sinha, L.; Pakhira, S.; Bhojane, P.; Mali, S.; Hong, C. K.; Shirage, P. M. Hybridization of Co_3O_4 and α-MnO_2 nanostructures for high-performance nonenzymatic glucose sensing. *ACS Sustainable Chem. Eng.* **2018**, *6*, 13248−13261.

(27) Zeng, Z.; Zhang, T.; Liu, Y.; Zhang, W.; Yin, Z.; Ji, Z.; Wei, J. Magnetic Field-Enhanced 4-Electron Pathway for Well-Aligned

Co$_3$O$_4$/Electrospun Carbon Nanofibers in the Oxygen Reduction Reaction. *ChemSusChem* **2018**, *11*, 580−588.

(28) Wang, Z.; Peng, S.; Hu, Y.; Li, L.; Yan, T.; Yang, G.; Ji, D.; Srinivasan, M.; Pan, Z.; Ramakrishna, S. Cobalt nanoparticles encapsulated in carbon nanotube-grafted nitrogen and sulfur co-doped multichannel carbon fibers as efficient bifunctional oxygen electrocatalysts. *J. Mater. Chem. A* **2017**, *5*, 4949−4961.

(29) Ji, L.; Wang, J.; Wu, K.; Yang, N. Tunable Electrochemistry of Electrosynthesized Copper Metal−Organic Frameworks. *Adv. Funct. Mater.* **2018**, *28*, No. 1706961.

(30) Li, Y.; Xie, M.; Zhang, X.; Liu, Q.; Lin, D.; Xu, C.; Xie, F.; Sun, X. Co-MOF nanosheet array: a high-performance electrochemical sensor for non-enzymatic glucose detection. *Sens. Actuators, B* **2019**, *278*, 126−132.

(31) Liu, X.; Li, M.; Han, G.; Dong, J. The catalysts supported on metallized electrospun polyacrylonitrile fibrous mats for methanol oxidation. *Electrochim. Acta* **2010**, *55*, 2983−2990.

(32) Liu, Y.; Zeng, Z.; Bloom, B.; Waldeck, D. H.; Wei, J. Stable Low-Current Electrodeposition of α-MnO$_2$ on Superaligned Electrospun Carbon Nanofibers for High-Performance Energy Storage. *Small* **2018**, *14*, No. 1703237.

(33) Aboagye, A.; Liu, Y.; Ryan, J. G.; Wei, J.; Zhang, L. Hierarchical carbon composite nanofibrous electrode material for high-performance aqueous supercapacitors. *Mater. Chem. Phys.* **2018**, *214*, 557−563.

(34) Mao, X.; Rutledge, G. C.; Hatton, T. A. Nanocarbon-based electrochemical systems for sensing, electrocatalysis, and energy storage. *Nano Today* **2014**, *9*, 405−432.

(35) Hu, L.; Chen, W.; Xie, X.; Liu, N.; Yang, Y.; Wu, H.; Yao, Y.; Pasta, M.; Alshareef, H. N.; Cui, Y. Symmetrical MnO$_2$−carbon nanotube−textile nanostructures for wearable pseudocapacitors with high mass loading. *ACS Nano* **2011**, *5*, 8904−8913.

(36) Liu, Y.; Huang, J.; Hou, H.; You, T. Simultaneous determination of dopamine, ascorbic acid and uric acid with electrospun carbon nanofibers modified electrode. *Electrochem. Commun.* **2008**, *10*, 1431−1434.

(37) Liu, Y.; Chen, Z.; Shek, C.-H.; Wu, C. L.; Lai, J. K. Hierarchical mesoporous MnO$_2$ superstructures synthesized by soft-interface method and their catalytic performances. *ACS Appl. Mater. Interfaces* **2014**, *6*, 9776−9784.

(38) Yang, S.; Liu, H.; Zhang, Y.; Wang, S.; Li, L.; Liu, X. Facile fabrication of hierarchical micro-meso-macro porous metal oxide with high photochemical and electrochemical performances. *Appl. Surf. Sci.* **2019**, *465*, 672−677.

(39) Wang, X.; Huo, S.; Wang, R.; Wang, H.; Brett, D. J.; Ji, S. Synthesis of high surface area mesoporous MnO$_2$ via a "metastable" aqueous interfacial reaction. *J. Colloid Interface Sci.* **2017**, *503*, 76−85.

(40) Liu, Y.; Zeng, Z.; Sharma, R. K.; Gbewonyo, S.; Allado, K.; Zhang, L.; Wei, J. A bi-functional configuration for a metal-oxide film supercapacitor. *J. Power Sources* **2019**, *409*, 1−5.

(41) Abdalla, I.; Shen, J.; Yu, J.; Li, Z.; Ding, B. Co3O4/carbon composite nanofibrous membrane enabled high-efficiency electromagnetic wave absorption. *Sci. Rep.* **2018**, *8*, No. 12402.

(42) Yang, Z.; Lv, J.; Pang, H.; Yan, W.; Qian, K.; Guo, T.; Guo, Z. Facile Synthesis of coaxial CNTs/MnO x-carbon hybrid nanofibers and their greatly enhanced lithium storage performance. *Sci. Rep.* **2015**, *5*, No. 17473.

(43) Fang, J.; Xie, Z.; Wallace, G.; Wang, X. Co-deposition of carbon dots and reduced graphene oxide nanosheets on carbon-fiber microelectrode surface for selective detection of dopamine. *Appl. Surf. Sci.* **2017**, *412*, 131−137.

(44) Zhao, Y.; Ran, W.; He, J.; Huang, Y.; Liu, Z.; Liu, W.; Tang, Y.; Zhang, L.; Gao, D.; Gao, F. High-performance asymmetric supercapacitors based on multilayer MnO$_2$/graphene oxide nanoflakes and hierarchical porous carbon with enhanced cycling stability. *Small* **2015**, *11*, 1310−1319.

(45) Qian, T.; Yu, C.; Zhou, X.; Ma, P.; Wu, S.; Xu, L.; Shen, J. Ultrasensitive dopamine sensor based on novel molecularly imprinted polypyrrole coated carbon nanotubes. *Biosens. Bioelectron.* **2014**, *58*, 237−241.

(46) Yen, S.-C.; Liu, Z.-W.; Juang, R.-S.; Sahoo, S.; Huang, C.-H.; Chen, P.; Hsiao, Y.-S.; Fang, J.-T. Carbon nanotube/conducting polymer hybrid nanofibers as novel organic bioelectronic interfaces for efficient removal of protein-bound uremic toxins. *ACS Appl. Mater. Interfaces* **2019**, *11*, 43843−43856.

(47) Li, X.; Shao, S.; Yang, Y.; Mei, Y.; Qing, W.; Guo, H.; Peng, L. E.; Wang, P.; Tang, C. Y. Engineering Interface with a One-Dimensional RuO$_2$/TiO$_2$ Heteronanostructure in an Electrocatalytic Membrane Electrode: Toward Highly Efficient Micropollutant Decomposition. *ACS Appl. Mater. Interfaces* **2020**, *12*, 21596−21604.

(48) Numan, A.; Shahid, M. M.; Omar, F. S.; Ramesh, K.; Ramesh, S. Facile fabrication of cobalt oxide nanograin-decorated reduced graphene oxide composite as ultrasensitive platform for dopamine detection. *Sens. Actuators, B* **2017**, *238*, 1043−1051.

(49) Yu, D.; Yao, J.; Qiu, L.; Wang, Y.; Zhang, X.; Feng, Y.; Wang, H. In situ growth of Co$_3$O$_4$ nanoparticles on α-MnO$_2$ nanotubes: a new hybrid for high-performance supercapacitors. *J. Mater. Chem. A* **2014**, *2*, 8465−8471.

(50) Gnana Kumar, G.; Awan, Z.; Nahm, K. S.; Xavier, J. S. Nanotubular MnO$_2$/graphene oxide composites for the application of open air-breathing cathode microbial fuel cells. *Biosens. Bioelectron.* **2014**, *53*, 528−534.

(51) Han, W.; Dong, F.; Han, W.; Tang, Z. Mn-Polyacrylonitrile Nanofibers Decorated with Co-Metal−Organic Frameworks as Precursors of CoMnOx Catalysts for the Combustion of Toluene. *ACS Appl. Nano Mater.* **2020**, *3*, 7818−7828.

(52) Ekoi, E. J.; Gowen, A.; Dorrepaal, R.; Dowling, D. P. Characterisation of titanium oxide layers using Raman spectroscopy and optical profilometry: Influence of oxide properties. *Results Phys.* **2019**, *12*, 1574−1585.

(53) Chen, S.; Zhu, J.; Wu, X.; Han, Q.; Wang, X. Graphene oxide−MnO$_2$ nanocomposites for supercapacitors. *ACS Nano* **2010**, *4*, 2822−2830.

(54) Jiang, H.; Yang, L.; Li, C.; Yan, C.; Lee, P. S.; Ma, J. High−rate electrochemical capacitors from highly graphitic carbon−tipped manganese oxide/mesoporous carbon/manganese oxide hybrid nanowires. *Energy Environ. Sci.* **2011**, *4*, 1813−1819.

(55) Ahmad, K.; Mohammad, A.; Mobin, S. M. Hydrothermally grown α-MnO$_2$ nanorods as highly efficient low cost counter-electrode material for dye-sensitized solar cells and electrochemical sensing applications. *Electrochim. Acta* **2017**, *252*, 549−557.

(56) Wang, J.; Gao, R.; Zhou, D.; Chen, Z.; Wu, Z.; Schumacher, G.; Hu, Z.; Liu, X. Boosting the electrocatalytic activity of Co$_3$O$_4$ nanosheets for a Li-O$_2$ battery through modulating inner oxygen vacancy and exterior Co3+/Co2+ ratio. *ACS Catal.* **2017**, *7*, 6533−6541.

(57) Yan, X.; Tian, L.; He, M.; Chen, X. Three-dimensional crystalline/amorphous Co/Co3O4 core/shell nanosheets as efficient electrocatalysts for the hydrogen evolution reaction. *Nano Lett.* **2015**, *15*, 6015−6021.

(58) Qiu, L.; Han, X.; Lu, Q.; Zhao, J.; Wang, Y.; Chen, Z.; Zhong, C.; Hu, W.; Deng, Y. Co$_3$O$_4$ Nanoparticles Supported on N-doped Electrospinning Carbon Nanofibers as an Efficient and Bifunctional Oxygen Electrocatalyst for Rechargeable Zn-Air Batteries. *Inorg. Chem. Front.* **2019**, *6*, 3554−3561.

(59) Tang, W.; Yao, M.; Deng, Y.; Li, X.; Han, N.; Wu, X.; Chen, Y. Decoration of one-dimensional MnO$_2$ with Co$_3$O$_4$ nanoparticles: a heterogeneous interface for remarkably promoting catalytic oxidation activity. *Chem. Eng. J.* **2016**, *306*, 709−718.

(60) Wang, J.-G.; Yang, Y.; Huang, Z.-H.; Kang, F. A high-performance asymmetric supercapacitor based on carbon and carbon−MnO$_2$ nanofiber electrodes. *Carbon* **2013**, *61*, 190−199.

(61) Ding, Y.; Wang, Y.; Su, L.; Bellagamba, M.; Zhang, H.; Lei, Y. Electrospun Co$_3$O$_4$ nanofibers for sensitive and selective glucose detection. *Biosens. Bioelectron.* **2010**, *26*, 542−548.

(62) Zhu, Q.; Li, Y.; Gao, Y.; Wang, X.; Song, S. Reduced Graphene-Wrapped MnO$_2$ Nanowires Self-Inserted with Co$_3$O$_4$ Nanocages:

Remarkable Enhanced Performances for Lithium-Ion Anode Applications. *Chem.-Eur. J.* **2016**, *22*, 6876−6880.

(63) Xiao, X.; Zhang, X.; Zhang, Z.; You, J.; Liu, S.; Wang, Y. Macro-/meso-porous NiCo 2 O 4 synthesized by template-free solution combustion to enhance the performance of a nonenzymatic amperometric glucose sensor. *Microchim. Acta* **2020**, *187*, 64.

(64) Mercante, L. A.; Pavinatto, A.; Iwaki, L. E.; Scagion, V. P.; Zucolotto, V.; Oliveira, O. N., Jr; Mattoso, L. H.; Correa, D. S. Electrospun polyamide 6/poly (allylamine hydrochloride) nanofibers functionalized with carbon nanotubes for electrochemical detection of dopamine. *ACS Appl. Mater. Interfaces* **2015**, *7*, 4784−4790.

(65) Zeng, Z.; Liu, Y.; Zhang, W.; Chevva, H.; Wei, J. Improved supercapacitor performance of MnO_2-electrospun carbon nanofibers electrodes by mT magnetic field. *J. Power Sources* **2017**, *358*, 22−28.

(66) Ma, W.; Chen, S.; Yang, S.; Chen, W.; Weng, W.; Cheng, Y.; Zhu, M. Flexible all-solid-state asymmetric supercapacitor based on transition metal oxide nanorods/reduced graphene oxide hybrid fibers with high energy density. *Carbon* **2017**, *113*, 151−158.

(67) Bazán, J. C.; Arvia, A. J. The diffusion of ferro-and ferricyanide ions in aqueous solutions of sodium hydroxide. *Electrochim. Acta* **1965**, *10*, 1025−1032.

(68) Zhang, E.; Xie, Y.; Ci, S.; Jia, J.; Wen, Z. Porous Co_3O_4 hollow nanododecahedra for nonenzymatic glucose biosensor and biofuel cell. *Biosens. Bioelectron.* **2016**, *81*, 46−53.

(69) Weina, X.; Guanlin, L.; Chuanshen, W.; Hu, C.; Wang, X. A novel β-MnO_2 micro/nanorod arrays directly grown on flexible carbon fiber fabric for high-performance enzymeless glucose sensing. *Electrochim. Acta* **2017**, *225*, 121−128.

(70) Liu, M.; Liu, R.; Chen, W. Graphene wrapped Cu_2O nanocubes: non-enzymatic electrochemical sensors for the detection of glucose and hydrogen peroxide with enhanced stability. *Biosens. Bioelectron.* **2013**, *45*, 206−212.

(71) Wei, J.; Liu, H.; Dick, A. R.; Yamamoto, H.; He, Y.; Waldeck, D. H. Direct Wiring of Cytochrome c's Heme Unit to an Electrode: Electrochemical Studies. *J. Am. Chem. Soc.* **2002**, *124*, 9591−9599.

(72) Palmer, M.; Masikini, M.; Jiang, L.-W.; Wang, J.-J.; Cummings, F.; Chamier, J.; Inyang, O.; Chowdhury, M. Enhanced electrochemical glucose sensing performance of CuO: NiO mixed oxides thin film by plasma assisted nitrogen doping. *J. Alloys Compd.* **2020**, *853*, No. 156900.

(73) Han, L.; Yang, D.-P.; Liu, A. Leaf-templated synthesis of 3D hierarchical porous cobalt oxide nanostructure as direct electrochemical biosensing interface with enhanced electrocatalysis. *Biosens. Bioelectron.* **2015**, *63*, 145−152.

(74) Ramasamy, R.; Ramachandran, K.; Philip, G. G.; Ramachandran, R.; Therese, H. A.; et al. Design and development of Co_3O_4/NiO composite nanofibers for the application of highly sensitive and selective non-enzymatic glucose sensors. *RSC Adv.* **2015**, *5*, 76538−76547.

(75) Moolayadukkam, S.; Thomas, S.; Sahoo, R. C.; Lee, C. H.; Lee, S. U.; Matte, H. R. Role of Transition Metals in Layered Double Hydroxides for Differentiating the Oxygen Evolution and Non-enzymatic Glucose Sensing. *ACS Appl. Mater. Interfaces* **2020**, *12*, 6193−6204.

(76) Lei, Y.; Butler, D.; Lucking, M. C.; Zhang, F.; Xia, T.; Fujisawa, K.; Granzier-Nakajima, T.; Cruz-Silva, R.; Endo, M.; Terrones, H.; et al. Single-atom doping of MoS_2 with manganese enables ultrasensitive detection of dopamine: Experimental and computational approach. *Sci. Adv.* **2020**, *6*, No. eabc4250.